

XCAT-3 : A Comprehensive Library of Personalized Digital Twins Derived from CT Scans

Lavsen Dahal^{a,b}, Mobina Ghoghnejad^a, Dhrubajyoti Ghosh^{a,c}, Yubraj Bhandari^a, David Kim^{a,b}, Fong Chi Ho^{a,b}, Fakrul Islam Tushar^{a,b}, Sheng Luo^{a,c}, Kyle J. Lafata^{a,b,d}, Ehsan Abadi^{a,b}, Ehsan Samei^{a,b}, Joseph Y. Lo^{a,b,+}, W. Paul Segars^{a,+}

^aCenter for Virtual Imaging Trials, Carl E. Ravin Advanced Imaging Laboratories, Department of Radiology, Duke University School of Medicine, Durham, NC, 27708, USA

^bElectrical and Computer Engineering, Pratt School of Engineering, Duke University, Durham, NC, 27708, USA

^cDepartment of Biostatistics & Bioinformatics, Duke University School of Medicine, Durham, NC, 27708, USA

^dDepartment of Radiation Oncology, Department of Radiology, Duke University School of Medicine, Durham, NC, 27708, USA

+These two authors contributed equally as Co-Senior Authors

ARTICLE INFO

Keywords: Computational Phantoms, Segmentation, Human Digital Twin, Computed Tomography, Neural Networks, Virtual Imaging Trials

ABSTRACT

Virtual Imaging Trials (VIT) offer a cost-effective and scalable approach for evaluating medical imaging technologies. Computational phantoms, which mimic real patient anatomy and physiology, play a central role in VITs. However, the current libraries of computational phantoms face limitations, particularly in terms of sample size and diversity. Insufficient representation of the population hampers accurate assessment of imaging technologies across different patient groups. Traditionally, computational phantoms were created by manual segmentation, which is a laborious and time-consuming task, impeding the expansion of phantom libraries. This study presents a framework for creating realistic computational phantoms using a suite of automatic segmentation models and performing three forms of automated

quality control on the segmented organ masks. The final result is the release of over 2500 computational phantoms with up to 140 structures, illustrating a comprehensive approach to detailed anatomical modeling. The developed computational phantoms are available in both voxelized and surface mesh formats. The framework is combined with an in-house CT scanner simulator to produce realistic CT images. The framework has the potential to advance virtual imaging trials, facilitating comprehensive and reliable evaluations of medical imaging technologies. Phantoms may be requested at <https://cvit.duke.edu/resources/>. Code, model weights, and sample CT images are available at <https://xcat-3.github.io/>.

1. Introduction

Virtual Imaging Trials (VIT) offer cost-effectiveness, speed and scalability in the evaluation and optimization of existing medical imaging technologies compared to traditional clinical trials [1-4]. VITs require a virtual patient population that mimics their anatomy and physiology. Such a virtual patient population can be created using computational anthropomorphic phantoms. These simulated phantoms are expected to represent the true population in terms of relevant trial characteristics such as body habitus, organ volumes, tissue properties, and blood flow.

There has been considerable efforts toward developing computational phantoms from geometric models in the 1960s [5] to more advanced surface-based models in recent years [6]. Many different phantoms have been developed over the years as summarized in [7, 8]. Despite this effort, the current phantom library sample size [9-12] is inadequate for use in certain virtual imaging studies where the required sample size is estimated to be in the thousands [13-15]. It is challenging to generate such a large number of

computational phantoms because phantom developments have, up to now, relied on manual organ segmentation, which is painstakingly slow, requires skilled expertise, and is still prone to human variability. Additionally, after segmentation, phantoms undergo multiple post-processing steps to ensure a precise 3D representation as surface models for various downstream tasks. This process is susceptible to errors and often necessitates significant manual intervention.

A recent approach by [16] aimed to automate phantom generation from radiological images but lacked quality due to insufficient performance of the implemented segmentation algorithm in terms of quality and number of organs segmented. However, recent advancements in deep learning have improved organ segmentations[17-21], enabling the creation of patient specific phantoms with accurate organ geometry representation. One segmentation algorithm which has gained popularity is TotalSegV2[17] which can identify 117 anatomical structures given 3D CT imaging data. The Segment Anything Model[20] is another such algorithm which excels in 2D segmentation [22]. Despite rapid advancements in the field, none of these models fully address the issues of segmentation failures or implement comprehensive quality control. Our major contributions are summarized below:

- **Segmentation with automated Quality Control:** We release a deep learning segmentation model (DukeSeg) capable of segmenting up to 140 structures integrated with automated quality control in three distinct ways to effectively address segmentation failures.
- **Person Specific Phantoms:** We offer over 2500 anatomical models in both voxel and high-resolution mesh output formats, each derived from actual patient data, which we call XCAT-3 models. These models are enriched with crucial metadata such as race, sex, age, and body habitus. This personalized dual-format approach is crucial for detailed anatomical studies, virtual imaging trials, surgical planning, and virtual reality simulations, allowing for smoother visualizations and more precise model interactions.

- **Automatic Pipeline for Phantom Generation:** We developed a fully automated pipeline for phantom generation as shown in Figure 1, which integrates multiple complex steps such as segmentation, quality control, meshing, and voxelization. Each of these methods is traditionally prone to various errors, but our scalable solution enables them to work together in an automated manner.

Methods

1.1 Data Curation

Four datasets with a total of 3400 CT volumes were used to develop the segmentation model, as presented in Table 1 and Table 2. The first set of data included the public dataset associated with TotalSegmentator [17] and a private dataset from the Duke University Health System, which were used for model development and validation, while three other public datasets were used for external testing: CT_ORG [23], ABDOMEN_1K [24], AMOS [25] and XCAT [10, 11]. To create computational phantoms comprehensive segmentation model was applied to a separate dataset of 3581 CT volumes from the Duke University Health System. The inclusion criteria for the dataset consisted of CT volumes acquired between January 1, 2014, and March 30, 2023, utilizing protocols that include PET/CT and chest-abdomen-pelvis scans, ensuring a comprehensive coverage of the whole body.

Our segmentation model training drew upon public and private data that were pseudo-labeled with a combination of public and private segmentation models. This approach allowed us to expand the training data and to incorporate a wider range of anatomical variations and complexities. The training data of 990 patient CT volumes comprised 489 patients selected from the 600 in the TotalSegmentator [17] dataset that contained full-body structures and 501 from the Duke CT dataset which were randomly sampled. For the TotalSegmentator cases, the provided labels were used. For the Duke data, pseudo-labels of organ masks were generated automatically using a combination of three models. The TotalSegmentator model

was used to label 104 structures while a proprietary commercial model was used to label 33 structures.

Additionally, the MOOSE public body composition model [21], created labels for visceral fat, subcutaneous fat, and muscles.

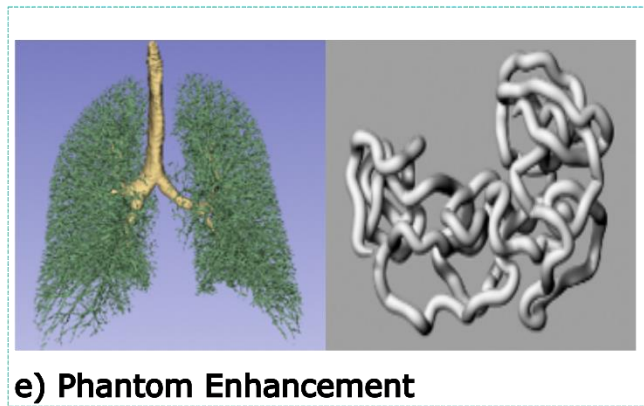
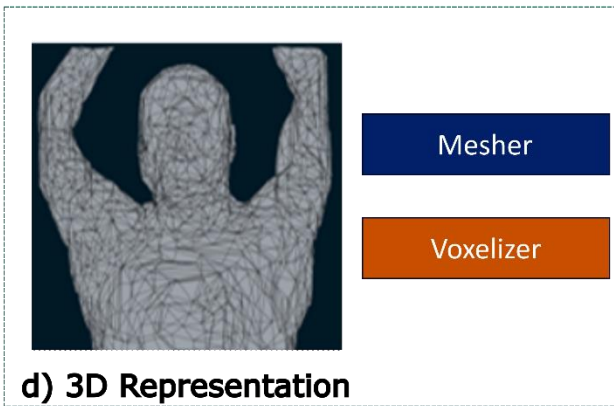
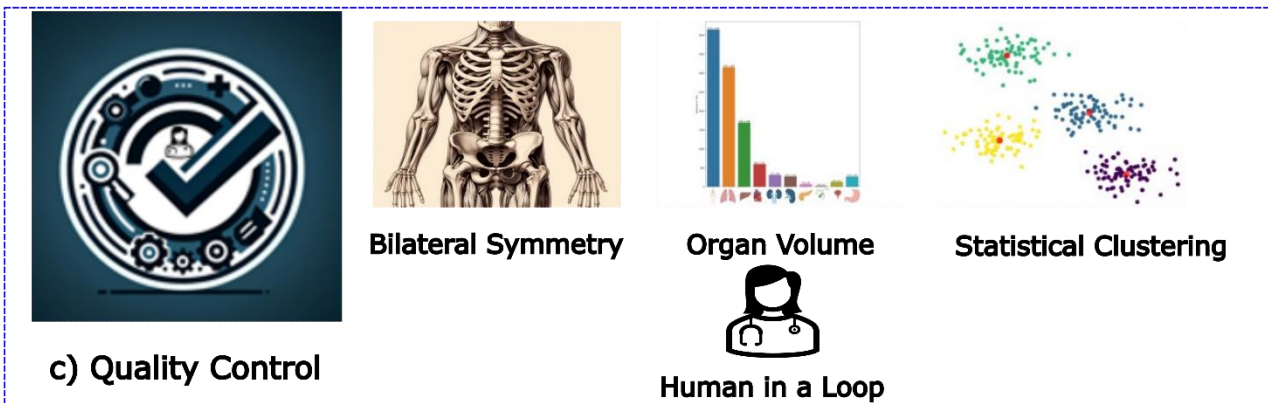
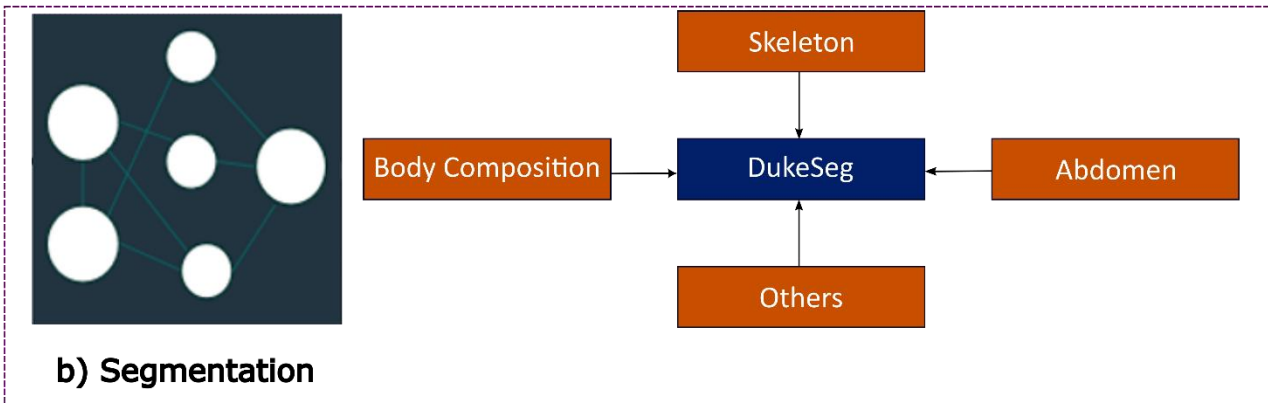
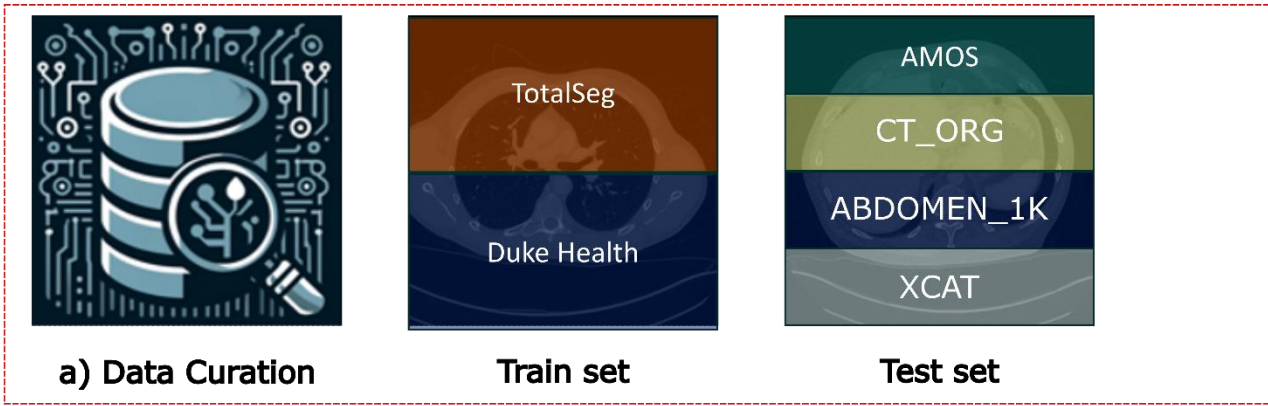


Figure 1. Overview of the Methodology: This figure illustrates the five-module approach used in our study. (a) Data Curation: Collect data from various public and private repositories to train and test the deep learning-based segmentation model, Dukeseq. (b) Dukeseq Model: An in-house developed segmentation tool consisting of four distinct models tailored for segmenting different anatomical structures. (c) Quality Control: Utilizes four types of quality assessments, validated by an MD to ensure accuracy through a human-in-the-loop approach. (d) 3D Representation: Represents the 3D segmentation results in mesh or voxel formats. (e) Detailed Modeling: Includes mathematical modeling of intricate anatomical details such as the small intestine, and airways and vessels.

<i>Table 1. Split for Train and Test utilizing various public and private datasets.</i>			<i>Table 2. Characteristics of Training set</i>		
Dataset	#Train	#Test	Dataset	Totalseg	DukeCT
TotalSegmentator	489	-	#Patients	489	501
DukeCT	501	-	Male	288	354
CT_ORG	-	140	Female	201	147
ABDOMEN_1K	-	1000	Age (years)	63.5(14.9)	62.1(16.3)
AMOS	-	200	Weight (kg)	-	86.5(23.1)
XCAT	-	50	Height (m)	-	1.73(0.10)
Total	990	1420	Slice thickness	1.5mm	0.625, 3.75 mm

1.2 Deep Learning Based Segmentation

The nnU-Net deep learning-based method [26] was trained as a set of four models, each specializing in segmenting different sets of structures. The first model segmented the body outline, subcutaneous fat, visceral fat, and muscles. The second model focused exclusively on bone segmentation, encompassing a set of 62 classes. The third model segmented a total of 13 classes focusing on the internal organs in the abdomen region and the esophagus. Meanwhile, the final model segmented 61 additional structures. In total, the four models cover a diverse range of anatomical structures.

1.3 Quality Control

With any segmentation approach, failures can occur due to factors like poor image quality or limitations of the model. To address this, we employed three quality control approaches: bilateral symmetry, volume

thresholding, and statistical outlier detection. First, by assuming bilateral symmetry in the skeletal system, differences in volume exceeding 50% indicate segmentation issues for symmetrical bones like ribs, clavicles, pelvis, and femurs. Up to two discrepancies among the 16 sets of symmetrical bones evaluated, which include 12 pairs of ribs and other paired skeletal structures were allowed. The bones of the arms were excluded due to position variations. Second, the organ volume is computed after segmentation and used to exclude patients with unusual positioning or incomplete scans based on more than 25% of segmented structures having zero volume. Third, in the statistical outlier detection method, Hartigan's dip test is applied to selected organs to determine if the volume distribution is multimodal. Outliers were identified in unimodal distributions by the interquartile range and in multimodal distributions by Gaussian mixture models. Organs with >90% outlier probabilities were flagged.

In our final quality control process, segmentation volumes rendered as 2D images were examined by a physician for any disparities. Any observed anomalies were flagged. This methodology exemplifies a 'human-in-the-loop' approach, combining expert oversight with technical optimizations for expedited yet thorough analysis.

1.4 3D Representation & Phantoms Smoothing

The Quality Control module employs stringent acceptance criteria to ensure high fidelity in segmentation results. Cases are rejected if they exhibit major faults, such as failures in bilateral symmetry, partial or incomplete scans as evidenced by volume checks, or failure in segmenting at least two organs identified by statistical clustering method. Only cases that pass these criteria proceed to the 3D representation module, where voxelized segmentation masks are transformed into smooth polygon meshes. For cases with minor irregularities, such as fewer segmented organs, these details are documented in the metadata along with a

quality rating from a medical doctor, ensuring that each model's accuracy and completeness are transparently communicated.

For mesh transformation, GPU-accelerated Laplacian smoothing was used to iteratively refine the vertex positions of 3D meshes while preserving their overall shapes. By utilizing a sparse adjacency matrix to represent mesh connectivity and incorporating a customizable smoothing weight, our approach allows for fine-tuning the degree of smoothing required. The algorithm, summarized below, begins by converting input mesh data into tensors. It then constructs edges, initializes edge weights, and creates a sparse adjacency matrix. Subsequently, row sums are computed for normalization, and the main smoothing loop iteratively updates vertex positions. Finally, the algorithm returns the smoothly refined phantom meshes, effectively achieving our goal of producing aesthetically pleasing, yet faithful, representations.

We developed a web application that showcases the developed phantoms interactively. This user-friendly application allows exploration of phantoms filtered by age, sex, and race, with options for random

selection and detailed examination of specific structures as shown in Figure 2.

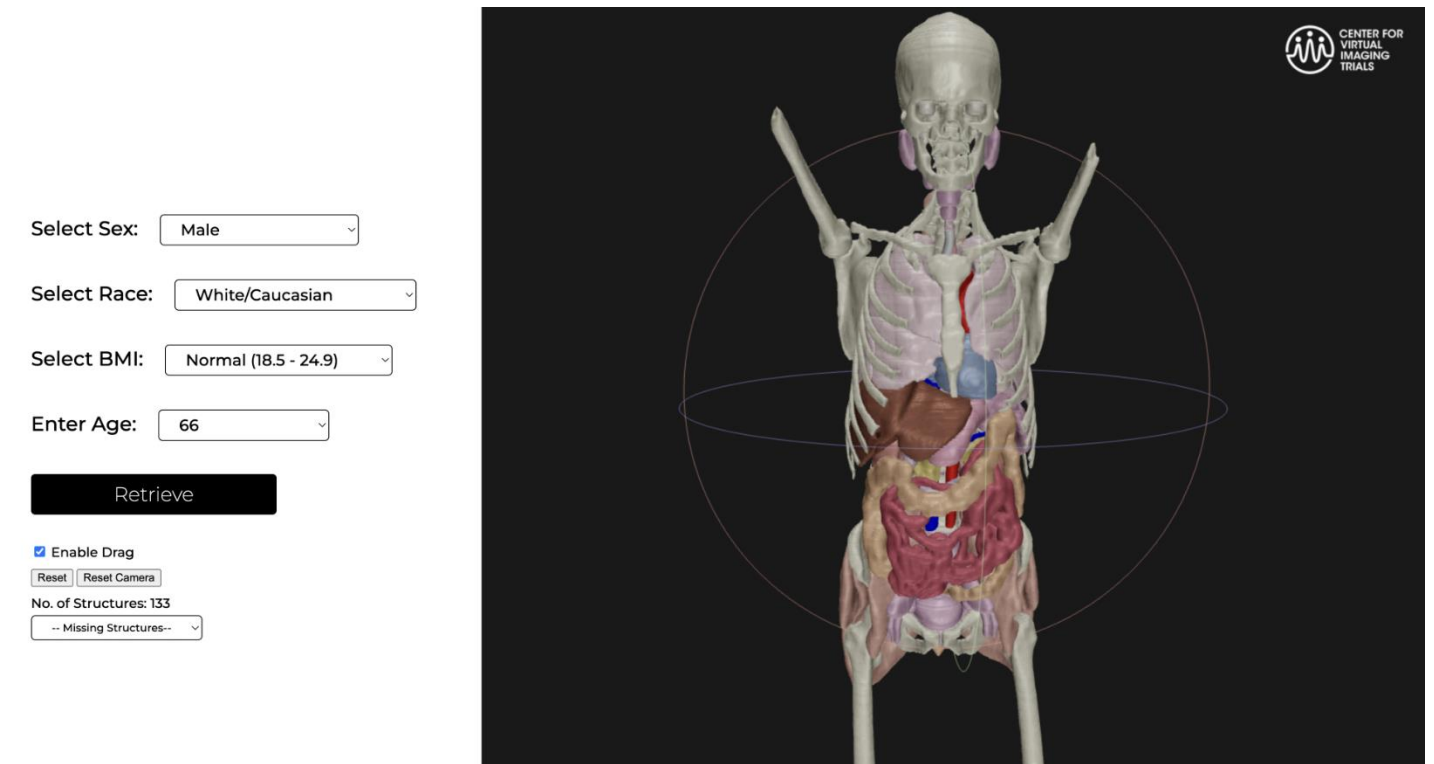


Figure 2. Web application that shows the 3d anatomical models while also allowing user interaction. The application can be accessed at <https://xcat-3.github.io>.

2.5 Phantom enhancements.

The basic phantoms consist of binary masks of the organs and structures, which can be optionally enhanced using techniques developed in our laboratory. Models for the cardiac and respiratory motion can be incorporated into the phantoms using the same techniques utilized to fit them within the XCAT series of adult and pediatric phantoms [10, 11].

A mathematical model [27] can be used to grow the airways and vessels within the lungs beyond those segmented. The new models extend from initially segmented branches to terminal branches, optimally distributing flow through the lungs while avoiding intersections between structures. Texture for the lung parenchyma can also be added to voxelized versions of the phantoms for increased anatomical detail [28].

To further enhance the bones, we developed an algorithm that will generate the inner trabecular bone structure with geometric and topological properties indicative of the individual bones [29]. The method is parameterized to model normal and abnormal variations.

Enhancement can also be performed for the small intestine. The small intestines can be refined using the gross segmentation of the small intestine to guide the procedural generation of a contiguous, tubular surface [30] [31] with a length, diameter, and mass within the range of normal values. The end result is a more realistic and flexible model for the intestine. The tubular surface can be easily manipulated to simulate respiratory or gastrointestinal motion [32].

In addition to the above, we have developed many different methods to model disease within computational phantoms such as those developed here. These diseases include emphysema[33], bronchitis[34], covid-19 pneumonia[35], cardiac plaques[36, 37], lung lesions[38, 39], and liver lesions[39]

2.6 Imaging Simulation using the Phantoms.

To generate simulated medical imaging scans, the phantoms produced through our pipeline may be input into imaging simulators[40-43] . One example is our in-house CT simulation platform (DukeSim) which has a hybrid approach for simulating CT projections using ray-tracing and Monte Carlo modules [43, 44].

DukeSim simulates a broad range of physics factors including different CT scanner designs and reconstruction algorithms. This simulation process culminates in the generation of highly detailed and realistic simulated CT images.

2. Results

3.1 Segmentation

The segmentation results are shown in box plots (Figure 3), indicating that our model performed similar to the other two models as evaluated using Dice similarity coefficient (DSC) between the predicted mask and the reference masks from respective datasets. The commercial model omitted structures that were only partially visible or had low confidence. To avoid skewing the plots, organs with DSC of 0 were removed. It should be noted that not all models could segment all structures; hence, not all structure DSC values could be reported. Furthermore, qualitative results for phantoms are presented in Figure 4.

3.2 Quality Control

To evaluate the quality of the phantoms, we implemented a multi-step quality control procedure. Initially, we excluded all the patients with age less than 14 years old as the segmentation algorithm was not effective for pediatric patients. The first step leveraged bone symmetry by flagging cases where contralateral bones are more than 50% dissimilar in volume. The method proved effective for preliminary screening: out of 3549 initial cases, 3499 or 99% met the 50% symmetry volume threshold.

The 3499 volumes from the first Quality Control set were passed to the volumetric evaluations of different organs. The goal was to exclude patients in which over 25% of the anatomical structures were missing – that is, organ volumes were zero – due to improper or insufficient scanning. This second step yielded 3406 patient CT scans that were subsequently converted into phantoms.

Among these 3406 patients, the statistical outlier detection approach provided the outlier probability for every organ of every patient. Figure 5 illustrates the average outlier probabilities for the top 10 organs, separated by sex. Notably, the gallbladder exhibited the highest outlier probability, missing in

approximately 16% of cases, predominantly due to cholecystectomies. The other significant outliers identified include the 12th ribs, portal and splenic veins, smaller structures such as the iliac arteries, and male-specific organs like the prostate and seminal vesicles. These findings align with the visual assessments conducted by the medical doctor.

Approximately 42% of the CT scans were acquired as full body PET/CT scans. The scans with incomplete or missing skull were identified based on outlier probabilities for three structures: brainstem, brain, and skull. Additional filtering was implemented to identify cases where more than two organs per patient exceeded an outlier probability threshold of 0.9, thereby flagging these volumes. Applying all these filters resulted in a curated collection of 3320 patients to provide the most complete, anatomically accurate phantoms. The number of volumes retained after each quality control step is summarized in Table 3. The filtered patients were not discarded, as they may still yield phantoms suitable for many studies. For example, the incomplete skull is irrelevant when creating chest phantoms for pulmonary analysis.

The final step in the process was to select a single volume for patients who have multiple CT volumes available. This was done by identifying the scan with the lowest average outlier probability for each patient who has more than two scans. Following this selection criterion, 2528 unique patients were retained.

Table 3. Volume Retention After Each Quality Control Step

Quality Control Step	Volumes Retained
Total Volumes Reviewed	3581
Age (≥ 14 years)	3549

Bilateral Symmetry	3499
Organ Volume	3406
Statistical Clustering	3320

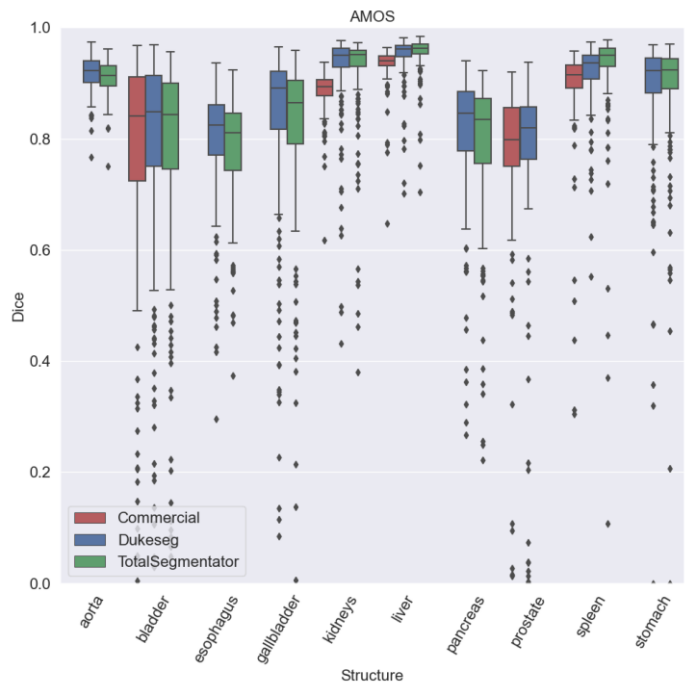
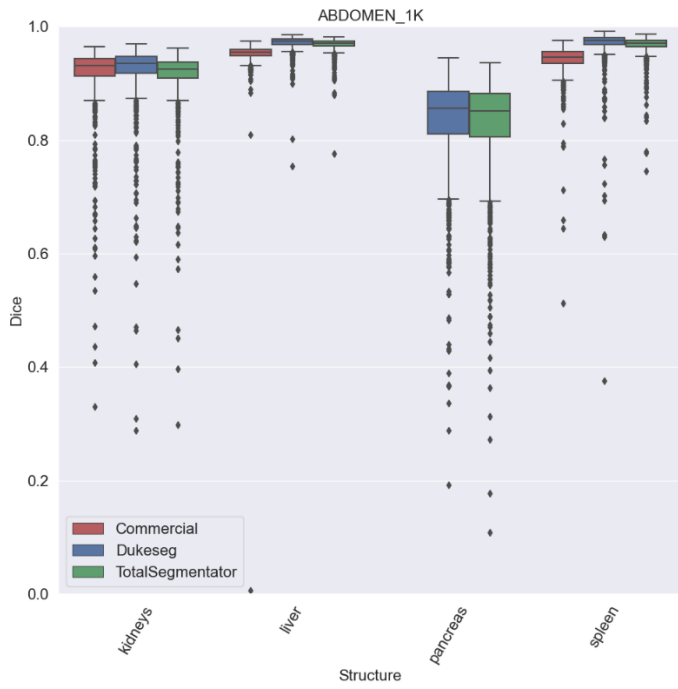
3.3 Patient Demographics and Composition.

In Figure 6 we present the demographic composition of the patient data used to generate the phantoms, reflecting the patient demographics of our institution. The population is primarily White, followed by Black, with a smaller representation of Asian individuals and other races categorized as 'Other'. Additionally, the reliance on PET/CT to provide whole body scans introduces a systematic bias, with a predominance of male subjects, likely attributable to the higher incidence of prostate and lung cancer among males. The average age for the male and female populations in the computational models are 64.9 (14.0) and 61.2 (15.6) years, respectively. Furthermore, a heatmap shown on Figure 7 represents the frequency of height and weight within the patient population from which the phantoms were created. Approximately $\frac{3}{4}$ of the patients were concentrated around weight between 70 and 100 kg and height between 1.7 and 1.9 meters. The physical traits that are most common among the patient cohort that contribute to the phantom dataset are shown in this visualization.

In Figure 8, we present the mean organ volume and standard deviation for selected organs across our phantom population. Notably, structures such as the gallbladder exhibit a significantly higher standard deviation, reflecting the variability of that small organ and the fact that some patients had undergone gallbladder removal surgery.

In **Error! Reference source not found.**, we present a range of phantoms that exhibit a wide variety of age, race, BMI, and sex characteristics to emphasize the diversity within our phantom collection. Muscles and fat have been omitted from these visualizations to maintain an unobstructed view of the internal anatomical

features. In the current iteration, bones located below the femur and other smaller bones have not been segmented.



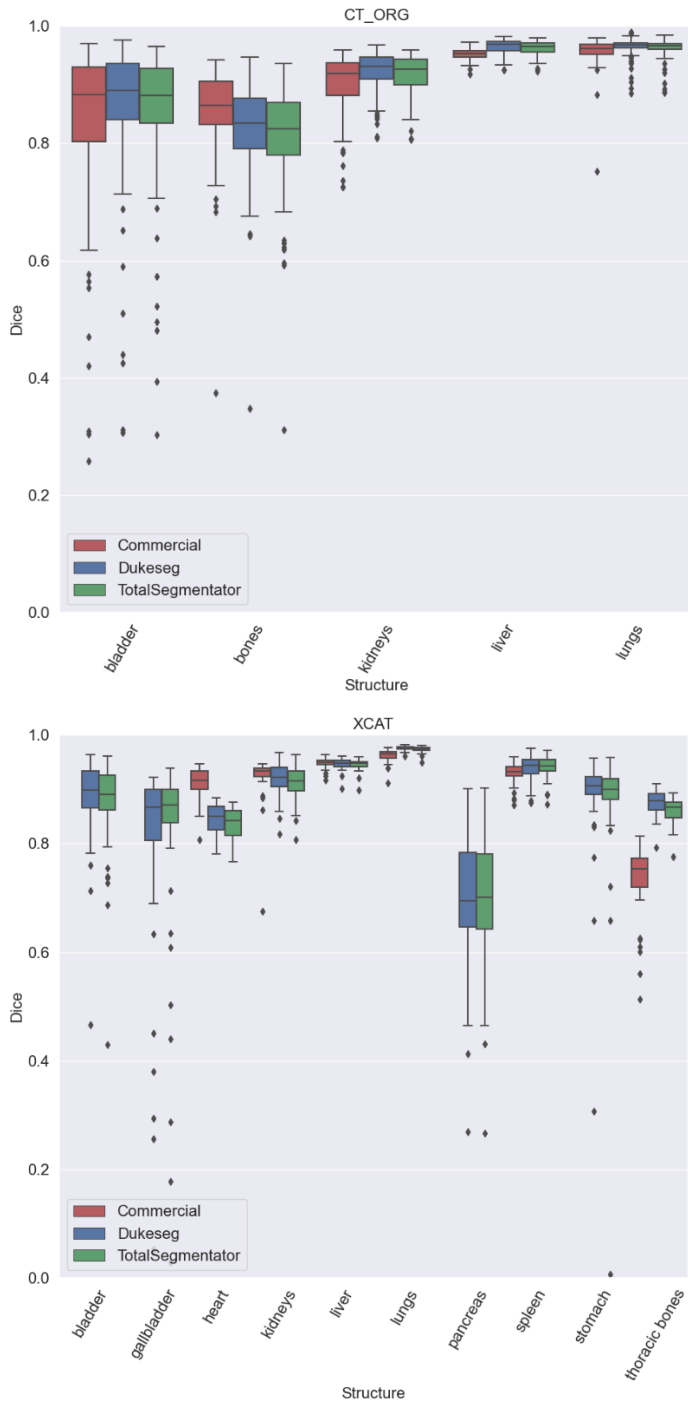


Figure 3. Boxplots that show the performance of DukeSeg compared with other public and private models. Performance is compared on three public datasets ABDOMEN_1K, AMOS, CT_ORG and a private dataset XCAT. Certain structures like ribs, scapula, and sternum were combined as thoracic bones for the XCAT dataset and minor structures such as the duodenum and adrenal glands were omitted for the AMOS dataset for clarity.

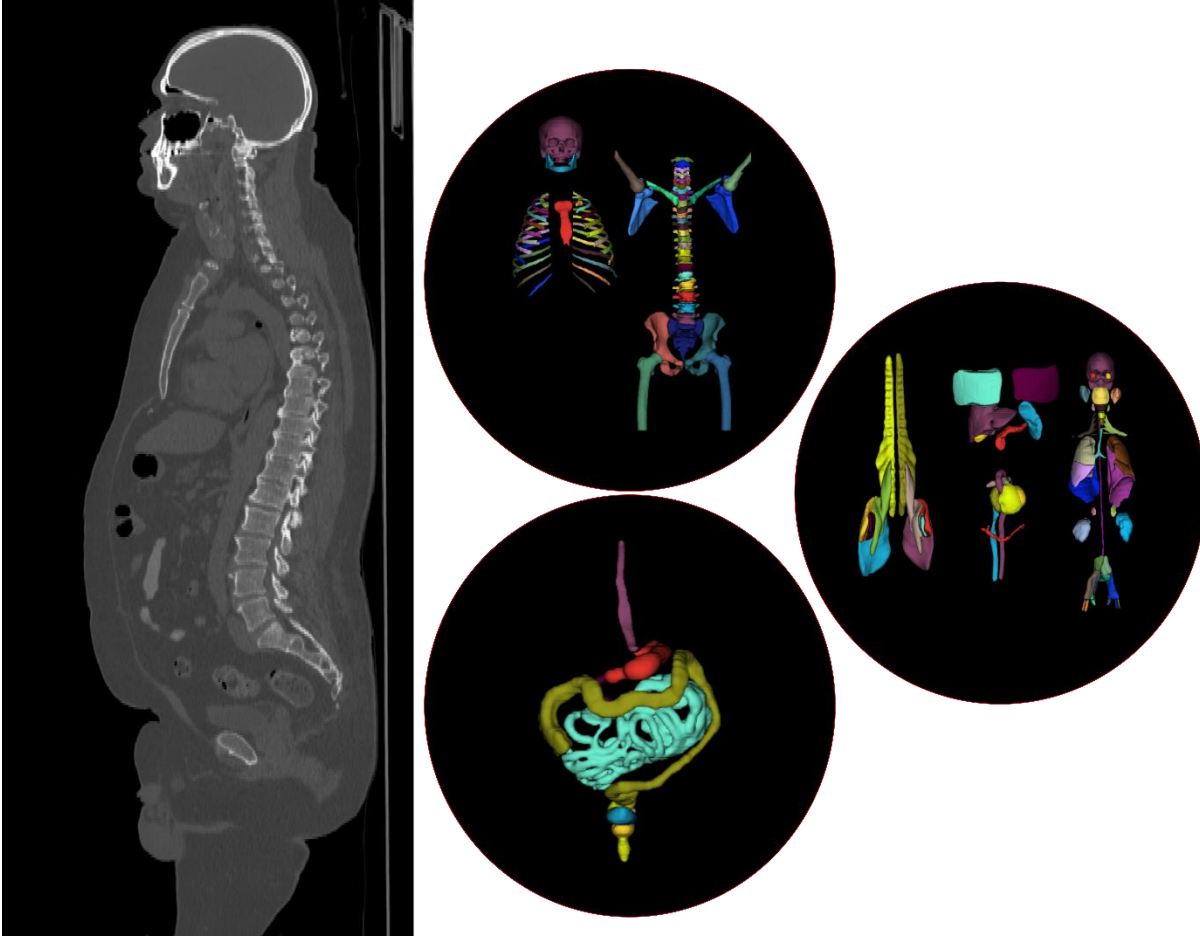


Figure 4. Qualitative comparison of segmentation results: the CT image is displayed on the left, with the outputs of the three segmentation models (Skeleton, Abdomen and Others) from Dukeseq illustrated in three circles on the right, showcasing their performance in delineating the targeted anatomical structures.

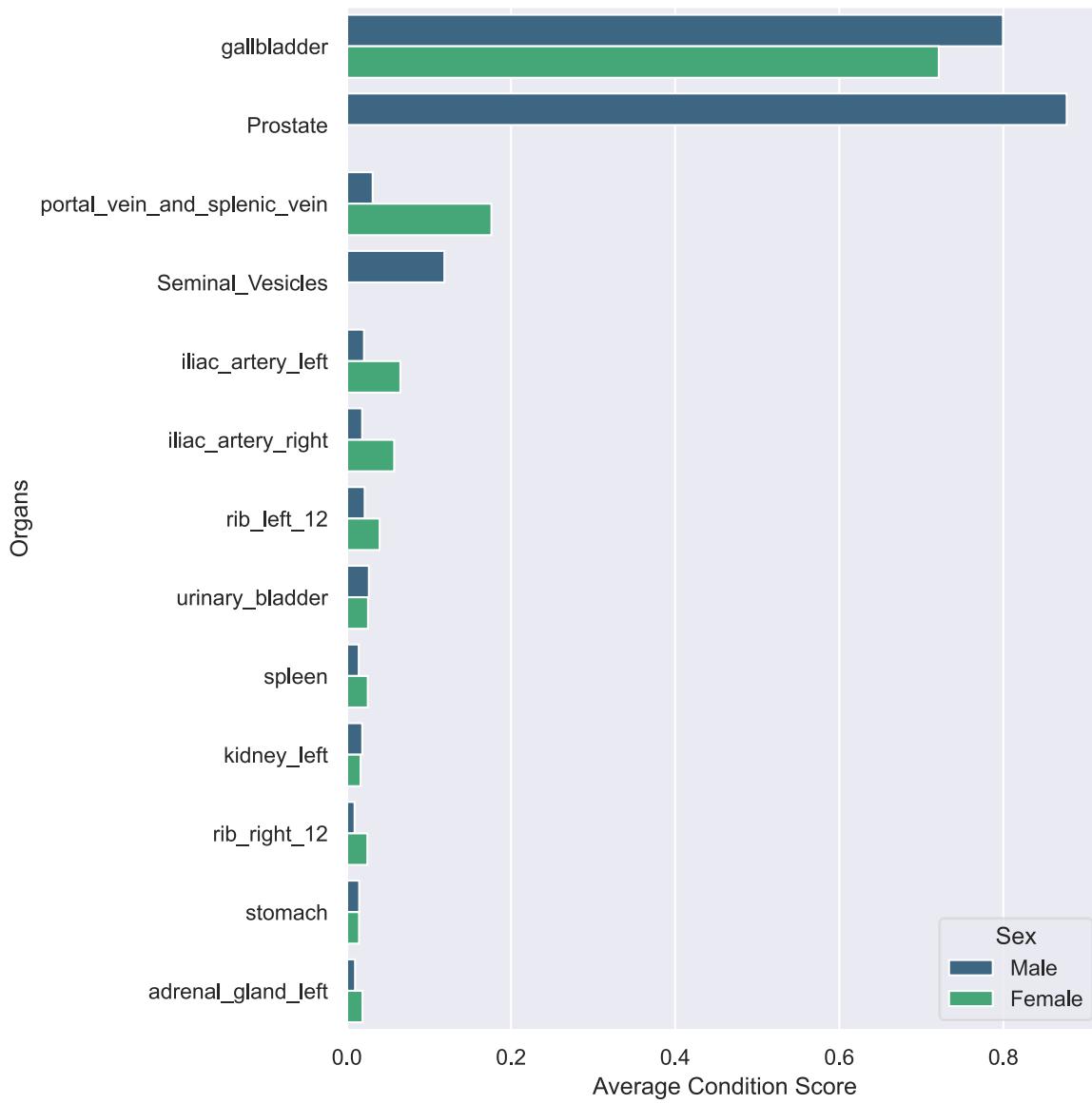


Figure 5. Top outlier organs identified by the Statistical Clustering approach for both sex.

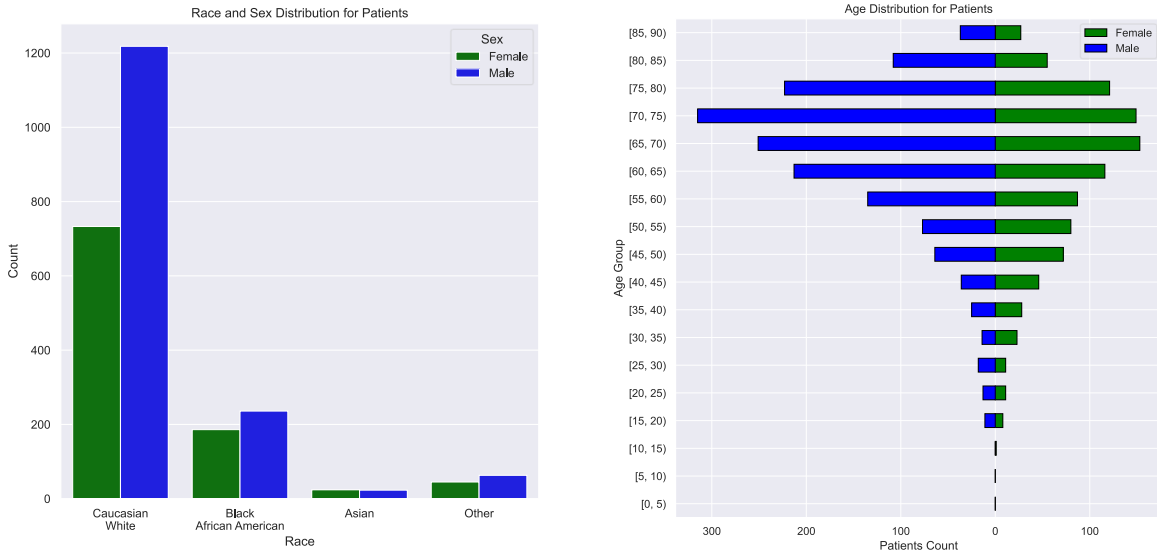


Figure 6. Race and Age distribution for the patients used to create the population of phantoms.

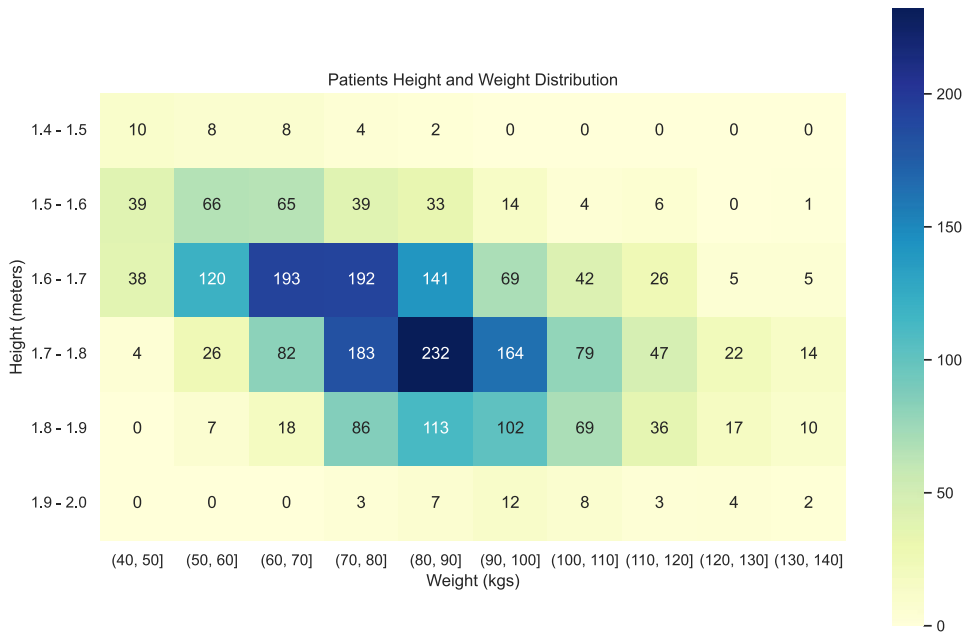


Figure 7. Height and Weight Distribution of the patients of the phantoms that passed all quality control measures used to create phantoms.

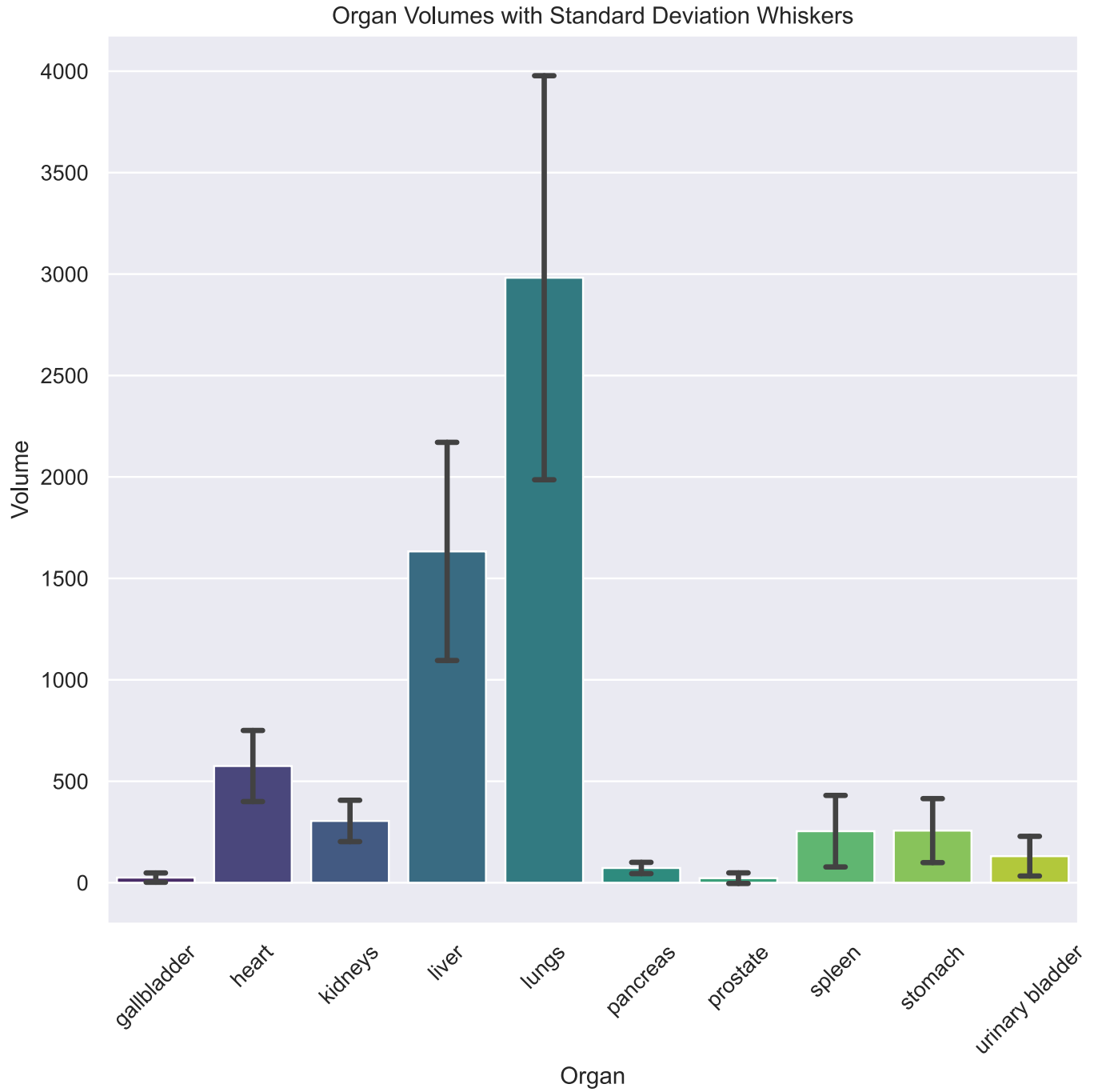


Figure 8. Organ volumes for major organs with range of mean and standard deviation.



Figure 9. 3D renderings of 4 computational phantoms in increasing order by height.

Discussion

In this study, we devised a framework for generating highly detailed patient-specific anatomical models, which represent a form of human digital twins appropriate for research in medical imaging. A significant challenge in scaling the phantom generation process was the manual segmentation of patient CT scans, which was prohibitively time-consuming and labor intensive. To overcome this bottleneck, we developed a deep learning model capable of segmenting up to 140 structures from patient CT volumes, which significantly enhanced the scalability of the phantom generation process. Furthermore, we implemented an automated quality control module to exclude or flag likely instances of segmentation failure, allowing the new phantoms to be based on the highest

quality subset while still preserving the larger population for applications suitable to the end user. This demonstration of scalability in phantom creation is crucial for use in virtual imaging trials, which necessitate a large and diverse sample size to ensure generalizability.

Building a fully automated segmentation pipeline poses significant challenges due to the inherent lack of high-quality image data with validated labels. Even widely used large CT datasets contain incorrect labels, which may limit segmentation model training as well as subsequent applications.

This study showed that quality control during the segmentation of 140 structures presents a formidable task due to the variations in size, shape, and appearance of these structures.

Consequently, a single quality control algorithm proved inadequate. For instance, a quality control measure that works for small structures like ribs may not be suitable for larger structures like the liver. The development of a multi-step quality control process improved the results for this study and may also benefit other segmentation studies.

We have employed a multi-model approach for segmenting the 140 structures, which offers two significant advantages. First, instead of retraining the entire model, we can selectively train only the model of interest. For instance, the skeletal system segmentation model achieved superior results, so we locked down this model early. However, there was still room for improvement in segmenting structures such as the large intestine and small intestine. Since these abdominal structures were segmented using the same model, we were able to focus on enhancing that specific model in further iterations. The second advantage of this design choice pertains to computational efficiency. Our studies involve full body CT scans, typically sized at 512x512x2000 for high resolution CTs at

0.625 mm resolution. Storing probabilities for 140 classes for each voxel becomes inconvenient in terms of scalability. Therefore, by employing multiple models, we mitigate the storage challenges associated with inferring and storing probabilities for the entire volume, thereby improving computational efficiency.

The web application developed to display diverse sets of anatomical models allows not only scientific inquiry but also may be helpful as an educational resource, introducing trainees and enthusiasts to detailed human anatomy through a dynamic and engaging platform. This initiative marks a significant stride in enhancing accessibility and interactivity in anatomical education.

Limitations and Future Work

Our phantoms are derived from CT images, which are obtained from patients undergoing medical evaluations rather than from the general healthy population. This selection bias presents a challenge in representing typical organ volumes accurately. Moreover, the reliance on PET/CT scans to provide whole body coverage led to more male patients. For many applications, the large size of the phantom cohort allows sub-sampling to mitigate these biases. The dataset included surgical removals such as for the gallbladder or kidney, which can be restored manually or by transforming from an anatomical template. Note however that our current patient-specific phantoms faithfully represent the actual patient anatomy.

Although the segmentation model was trained and validated on multiple datasets, the final phantoms were created only using data from the Duke University Health System. It is challenging to

acquire large clinical datasets that include CT images, radiologist reports to guide the quality control, as well as demographic/clinical data. This restriction means the generated phantoms predominantly represent the demographic distribution of one academic institution in the southeastern US, which may not reflect broader demographics. To address this issue and enhance the model's generalizability, future efforts will aim to validate our segmentation model using a more diverse dataset from multiple medical centers. Future studies will expand the scope to improve segmentation techniques and integrate more structures into the computational model by refining the segmentation algorithm or incorporating generative methods to fill in anatomical gaps.

Conclusion

We developed a pipeline to build computational phantoms using deep learning techniques integrated with stringent quality control. We designed an interactive web application with the power to filter and display phantoms by age, sex, and race. These phantoms will facilitate the conducting of virtual imaging trials in a wide range of clinical applications. This versatility underscores the potential of our phantoms to revolutionize virtual trials and beyond, offering a wide range of possibilities for research and development in the field of medical imaging.

Data availability

The anthropomorphic phantoms may be requested at <https://cvit.duke.edu/resources/>.

Code availability.

The code for generating phantoms, which encompasses segmentation, quality control (QC), and meshing, is available at <https://xcat-3.github.io/>. Modules for enhancing phantoms, including the addition of lesions and tissue textures, as well as CT simulation packages, are accessible upon request for research purposes.

Acknowledgments

This work was funded by the Center for Virtual Imaging Trials, NIH/NIBIB P41EB028744, NIH/NIBIB EB001838 and NIH/NCI R01CA261457.

References

1. Barufaldi, B., et al., *Virtual clinical trials in medical imaging system evaluation and optimisation*. Radiation Protection Dosimetry, 2021. **195**(3-4): p. 363-371.
2. Tushar, F.I., et al., *Data diversity and virtual imaging in AI-based diagnosis: A case study based on COVID-19*. arXiv preprint arXiv:2308.09730, 2023.
3. Tushar, F.I., et al. *Virtual NLST: towards replicating national lung screening trial*. in *Medical Imaging 2024: Physics of Medical Imaging*. 2024. SPIE.
4. Abadi, E., et al., *Virtual clinical trials in medical imaging: a review*. Journal of Medical Imaging, 2020. **7**(4): p. 042805-042805.
5. Fisher Jr, H., *Variation of dose delivered by ^{137}Cs as a function of body size from infancy to adulthood*. ORNL-4007, 1966: p. 221-228.
6. Segars, W.P., et al., *4D XCAT phantom for multimodality imaging research*. Medical physics, 2010. **37**(9): p. 4902-4915.
7. Bolch, W., *Computational models of human anatomy*, in *Monte Carlo Calculations in Nuclear Medicine (Second Edition) Therapeutic applications*. 2022, IOP Publishing Bristol, UK. p. 5-1-5-43.
8. Akhavanallaf, A., et al., *An update on computational anthropomorphic anatomical models*. Digital Health, 2022. **8**: p. 20552076221111941.
9. Lee, C., et al., *The UF family of reference hybrid phantoms for computational radiation dosimetry*. Physics in Medicine & Biology, 2009. **55**(2): p. 339.
10. Segars, W., et al., *The development of a population of 4D pediatric XCAT phantoms for imaging research and optimization*. Medical physics, 2015. **42**(8): p. 4719-4726.

11. Segars, W., et al., *Population of anatomically variable 4D XCAT adult phantoms for imaging research and optimization*. Medical physics, 2013. **40**(4): p. 043701.
12. Chen, Y., et al., *Construction of Chinese adult male phantom library and its application in the virtual calibration of in vivo measurement*. Physics in Medicine & Biology, 2016. **61**(5): p. 2124.
13. Young, S., et al., *A virtual trial framework for quantifying the detectability of masses in breast tomosynthesis projection data*. Medical physics, 2013. **40**(5): p. 051914.
14. Fukunaga, K. and R.R. Hayes, *Effects of sample size in classifier design*. IEEE Transactions on Pattern Analysis and Machine Intelligence, 1989. **11**(8): p. 873-885.
15. Park, S., G. Zhang, and K.J. Myers, *Comparison of channel methods and observer models for the task-based assessment of multi-projection imaging in the presence of structured anatomical noise*. IEEE transactions on medical imaging, 2016. **35**(6): p. 1431-1442.
16. Fu, W., et al., *iPhantom: a framework for automated creation of individualized computational phantoms and its application to CT organ dosimetry*. IEEE journal of biomedical and health informatics, 2021. **25**(8): p. 3061-3072.
17. Wasserthal, J., et al., *Totalsegmentator: Robust segmentation of 104 anatomic structures in ct images*. Radiology: Artificial Intelligence, 2023. **5**(5).
18. Liu, J., et al. *Clip-driven universal model for organ segmentation and tumor detection*. in *Proceedings of the IEEE/CVF International Conference on Computer Vision*. 2023.
19. Kirillov, A., et al. *Segment anything*. in *Proceedings of the IEEE/CVF International Conference on Computer Vision*. 2023.
20. Ma, J., et al., *Segment anything in medical images*. Nature Communications, 2024. **15**(1): p. 654.
21. Sundar, L.K.S., et al., *Fully automated, semantic segmentation of whole-body 18F-FDG PET/CT images based on data-centric artificial intelligence*. Journal of Nuclear Medicine, 2022. **63**(12): p. 1941-1948.
22. Mazurowski, M.A., et al., *Segment anything model for medical image analysis: an experimental study*. Medical Image Analysis, 2023. **89**: p. 102918.
23. Rister, B., et al., *CT-ORG, a new dataset for multiple organ segmentation in computed tomography*. Scientific Data, 2020. **7**(1): p. 381.
24. Ma, J., et al., *Abdomenct-1k: Is abdominal organ segmentation a solved problem?* IEEE Transactions on Pattern Analysis and Machine Intelligence, 2021. **44**(10): p. 6695-6714.
25. Ji, Y., et al., *Amos: A large-scale abdominal multi-organ benchmark for versatile medical image segmentation*. Advances in Neural Information Processing Systems, 2022. **35**: p. 36722-36732.
26. Isensee, F., et al., *nnU-Net: a self-configuring method for deep learning-based biomedical image segmentation*. Nature methods, 2021. **18**(2): p. 203-211.
27. Abadi, E., et al., *Modeling lung architecture in the XCAT series of phantoms: physiologically based airways, arteries and veins*. IEEE transactions on medical imaging, 2017. **37**(3): p. 693-702.
28. Abadi, E., et al. *Airways, vasculature, and interstitial tissue: anatomically informed computational modeling of human lungs for virtual clinical trials*. in *Medical Imaging 2017: Physics of Medical Imaging*. 2017. SPIE.

29. Sauer, T.J., et al., *Surface-based anthropomorphic bone structures for use in high-resolution simulated medical imaging*. *Physics in Medicine & Biology*, 2023. **69**(1): p. 015023.
30. Yeom, Y.S., et al., *New small-intestine modeling method for surface-based computational human phantoms*. *Journal of Radiological Protection*, 2016. **36**(2): p. 230.
31. Kim, D., et al. *Random walk small intestine models for virtual patient populations*. in *Medical Imaging 2024: Physics of Medical Imaging*. 2024. SPIE.
32. Subashi, E., et al., *A model for gastrointestinal tract motility in a 4D imaging phantom of human anatomy*. *Medical physics*, 2023. **50**(5): p. 3066-3075.
33. Abadi, E., et al., *Emphysema quantifications with CT: Assessing the effects of acquisition protocols and imaging parameters using virtual imaging trials*. *Chest*, 2022.
34. Ho, F.C., et al. *Development and application of a virtual imaging trial framework for airway quantifications via CT*. in *Medical Imaging 2023: Physics of Medical Imaging*. 2023. SPIE.
35. Abadi, E., et al., *Virtual imaging trials for coronavirus disease (COVID-19)*. *AJR. American journal of roentgenology*, 2021. **216**(2): p. 362.
36. Sauer, T.J., et al. *Optimization of CT angiography using physiologically-informed computational plaques, dynamic XCAT phantoms, and physics-based CT simulation*. in *Medical Imaging 2021: Physics of Medical Imaging*. 2021. SPIE.
37. Sauer, T.J., et al. *Synthesis of physiologically-informed computational coronary artery plaques for use in virtual clinical trials (Conference Presentation)*. in *Medical Imaging 2020: Physics of Medical Imaging*. 2020. SPIE.
38. Sauer, T.J., et al., *Development and CT image-domain validation of a computational lung lesion model for use in virtual imaging trials*. *Medical Physics*, 2023.
39. Solomon, J. and E. Samei, *A generic framework to simulate realistic lung, liver and renal pathologies in CT imaging*. *Physics in Medicine & Biology*, 2014. **59**(21): p. 6637.
40. De Man, B., et al. *CatSim: a new computer assisted tomography simulation environment*. in *Medical Imaging 2007: Physics of Medical Imaging*. 2007. SPIE.
41. Badal, A. and A. Badano, *Accelerating Monte Carlo simulations of photon transport in a voxelized geometry using a massively parallel graphics processing unit*. *Medical physics*, 2009. **36**(11): p. 4878-4880.
42. Barufaldi, B., et al. *OpenVCT: a GPU-accelerated virtual clinical trial pipeline for mammography and digital breast tomosynthesis*. in *Medical Imaging 2018: Physics of Medical Imaging*. 2018. SPIE.
43. Abadi, E., et al., *DukeSim: a realistic, rapid, and scanner-specific simulation framework in computed tomography*. *IEEE transactions on medical imaging*, 2018. **38**(6): p. 1457-1465.
44. Sharma, S., et al., *A GPU-accelerated framework for rapid estimation of scanner-specific scatter in CT for virtual imaging trials*. *Physics in Medicine & Biology*, 2021. **66**(7): p. 075004.